PHILOSOPHICAL TRANSACTIONS OF THE ROYAL SOCIETY B

rstb.royalsocietypublishing.org

Research

Cite this article: Medvedev N, Popov V, Henneberger C, Kraev I, Rusakov DA, Stewart MG. 2014 Glia selectively approach synapses on thin dendritic spines. *Phil. Trans. R. Soc. B* **369**: 20140047.
http://dx.doi.org/10.1098/rstb.2014.0047

One contribution of 23 to a Theme Issue 'Brain circuitry outside the synaptic cleft'.

Subject Areas:
neuroscience

Keywords:
glia protection, synapses, thin spines

Authors for correspondence:
Dmitri A. Rusakov
e-mail: d.rusakov@ion.ucl.ac.uk
Michael G. Stewart
e-mail: m.g.stewart@open.ac.uk

†Deceased 28 January 2011.

Electronic supplementary material is available at http://dx.doi.org/10.1098/rstb.2014.0047 or via http://rstb.royalsocietypublishing.org.

Royal Society Publishing

Glia selectively approach synapses on thin dendritic spines

Nikolai Medvedev[1], Victor Popov[1,2,†], Christian Henneberger[3,4], Igor Kraev[1], Dmitri A. Rusakov[3] and Michael G. Stewart[1]

[1]Department of Life and Health Sciences, The Open University, Milton Keynes MK7 6AA, UK
[2]Institute of Cell Biophysics, Russian Academy of Sciences, Pushchino 142290, Russia
[3]Institute of Neurology, University College London, Queen Square, London WC1N 3BG, UK
[4]Institute of Cellular Neurosciences, University of Bonn Medical School, Bonn, Germany

This paper examines the relationship between the morphological modality of 189 dendritic spines and the surrounding astroglia using full three-dimensional reconstructions of neuropil fragments. An integrative measure of three-dimensional glial coverage confirms that thin spine postsynaptic densities are more tightly surrounded by glia. This distinction suggests that diffusion-dependent synapse–glia communication near 'learning' synapses (associated with thin spines) could be stronger than that near 'memory' synapses (associated with larger spines).

1. Introduction

In the hippocampus, high-affinity transporters populating astroglia membranes rapidly buffer the excitatory neurotransmitter glutamate released by synaptic discharges [1–4]. This powerful uptake system maintains low ambient extracellular glutamate (20–30 nM), providing a 'silent' background for transient excitatory signals [5]. However, astrocytes occupy less than 10% of tissue volume in area CA1 of the hippocampus [6], and synchronous synaptic releases may give rise to extra- or inter-synaptic actions of glutamate [7–9]. Indeed, astrocyte protrusions occur unevenly in the hippocampal neuropil, closely approaching only 20–30% of excitatory synapses [10], with no apparent relationship to the morphology of the host dendritic spines [11]. However, glial coverage of synapses varies depending on the organism's physiological state [12,13], which raises the question as to whether there is an adaptive significance for the uneven distribution of astroglia near hippocampal synapses.

To investigate this, we first documented the architectonics and the tissue volume fraction occupied by live astrocytes in dentate neuropil and, second, reconstructed in three dimensions the ultrastructure of contiguous astrocyte fragments together with the adjacent excitatory synapses. To quantify juxtaposition of synapses and astroglia, we first calculated the shortest distances between astrocyte membranes and the nearest edges of postsynaptic densities (PSDs) at 136 'thin' and 53 'mushroom' dendritic spines [14,15] of dentate granule cells. Second, we applied an integrative weighted-distance measure providing cumulative data about spatial glial coverage of PSDs. We found that glial membranes occur substantially closer to the PSDs of thin dendritic spines compared with mushroom spines. Because mushroom and thin dendritic spines have been associated with the different dominant synaptic receptors [16–18] and different stages of synaptic plasticity [19–21] (although see [22]), the results suggest that glia may selectively approach synapses that are in the process of physiological 'learning'.

2. Material and methods

(a) Two-photon microscopy and morphometry

Acute 350 μm slices from male Wistar rats (approx. eight-week-old) were transferred to the recording submersion chamber (Scientific Systems Design, NJ, USA) in an

© 2014 The Authors. Published by the Royal Society under the terms of the Creative Commons Attribution License http://creativecommons.org/licenses/by/4.0/, which permits unrestricted use, provided the original author and source are credited.

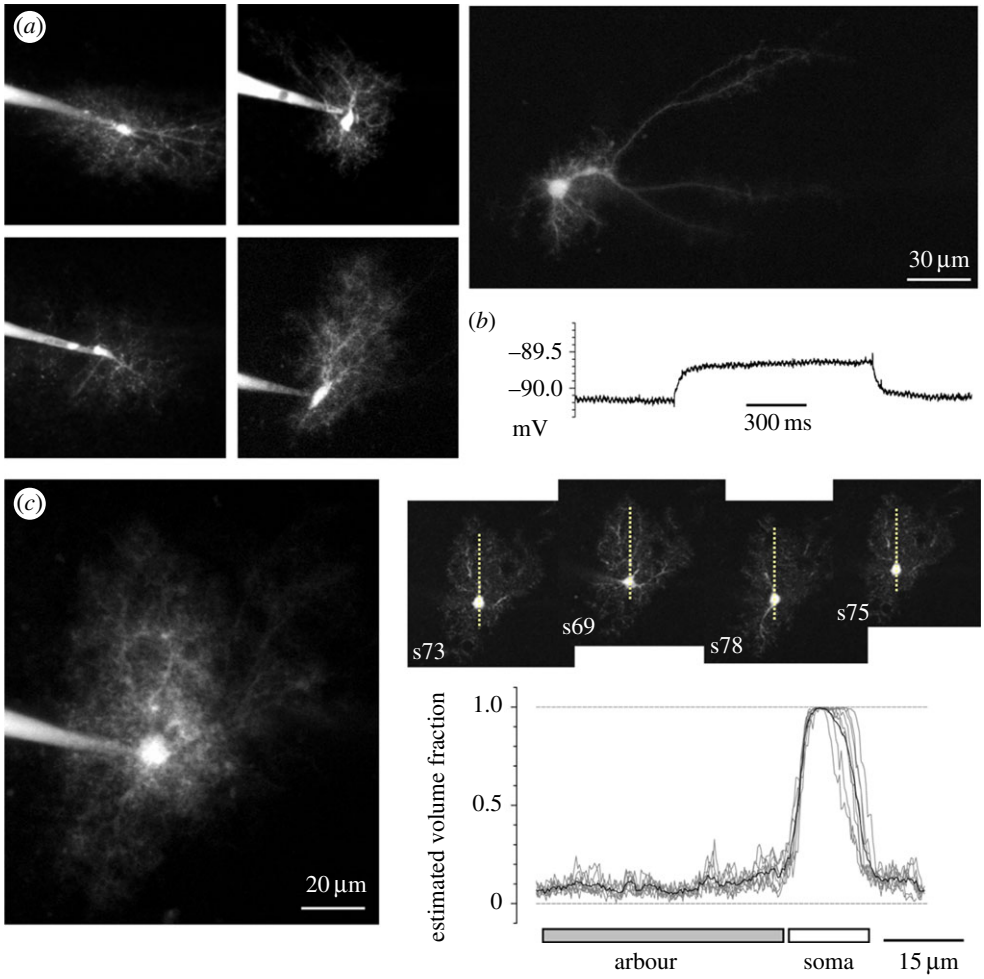

Figure 1. Morphology of live astrocytes in dentate gyrus. (*a*) Characteristic morphologies of individual astrocytes held in whole-cell mode and filled with Alexa Fluor 594 ($\lambda_x = 800$ nm); each fluorescence image represents an averaged *Z*-stack of 70–110 consecutive *X*–*Y* two-photon excitation sections taken with 0.5 µm *Z*-axis steps; patch pipettes are seen. Image on far right, an astrocyte representing a sub-group with prominent dendritic trunks [24]. (*b*) Input resistance measurement in a typical 'passive' astrocyte; whole-cell current clamp mode, a voltage response to a 200 pA current injection pulse is shown (upper trace; also see text and electronic supplementary material, figure S1). (*c*) In each astrocyte, distribution of the tissue volume fraction G_V^{min} occupied by thin, indicator-filled astrocyte processes (excluding areas containing large dendritic trunks) is measured in a *Z*-series of thin *X*–*Y* optical sections provided by two-photon excitation. Left panel, an image stack average (as in (*a*)). Right inset panels, examples of individual *X*–*Y* sections (section number reference is indicated; the effective optical width, approx. 1 µm) containing the soma; dotted line, a sampling segment (example) for the fluorescence brightness profile. Such samples were taken systematically in each *X*–*Y* section, normally by rotating the sampling segment in approximately 20° increments around the soma, throughout the Z-stack containing the soma. Plot, an example of G_V^{min} measurements in eight different *X*–*Y* sections of the same astrocyte (shown on the left): brightness profiles are normalized with respect to the brightness level inside the soma (see text) within each *X*–*Y* section; grey, individual profiles; black, average. Gap junctions are blocked with carbenoxolone (Material and methods).

Olympus microscope integrated with a BioRad Radiance 2100 imaging system and coupled with a femtosecond-infrared laser (MaiTai, SpectraPhysics) and patch-clamp electrophysiology [23]. The superfusion solution contained (mM): 124 NaCl, 2 KCl, 2 $CaCl_2$, 1 $MgCl_2$, 10 glucose, bubbled with 95%/5% of O_2/CO_2. Astrocytes in dentate gyrus were held in whole-cell mode; the internal solution contained (mM): 135 K methanesulfonate, 10 HEPES, 10 Na_2 phosphocreatine, 4 $MgCl_2$, 4 NaATP, 0.4 NaGTP and 40 µM Alexa Fluor 594 (MW 759; chosen to ensure rapid morphological tracing of thin processes, and because it provides 100% staining of thin processes and even penetrates gap junctions). Pipette resistance was 3–4 MOhm, access resistance less than 15 MOhm. Passive astrocytes were identified electrophysiologically as non-excitable, low-input-resistance cells; this was subsequently verified by observing cell morphology (Results, figure 1). Dye escape through gap junctions was prevented by adding 100 µM carbenoxolone to the bath. The potential effect of carbenoxolone on fine glial morphology was tested in a homogeneous population of CA1 astrocytes: the mean tissue volume fraction (Results) in the control and carbenoxolone samples were, respectively, 0.0732 ± 0.0088 and 0.0728 ± 0.0096 (mean ± s.e.; $n = 15$ and 8; $p > 0.95$), indicating no effect of the drug. The laser beam intensity under the objective was less than 8 mW, to avoid any photobleaching of Alexa [23]. In each astrocyte, the emission intensity data were collected using a *Z*-series of thin two-photon excitation layers (approx. 1 µm thick; optical resolution in the *X*–*Y* plane was 0.4–0.6 µm). The original brightness levels were preserved throughout.

(b) Tissue preparation and processing for electron microscopy

Animals were anaesthetized (urethane 1.5 g kg^{-1}), perfused transcardially with 100 ml saline, followed by 100 ml 3.5% paraformaldehyde and 0.5% glutaraldehyde (0.1 M Na cacodylate buffer, pH 7.4) at room temperature (RT, 22°C). After perfusion, the brains were removed and coronal serial 50-µm sections were cut from each brain containing the whole dorsal portion of the hippocampus. Slices were immersed in 2.5% glutaraldehyde (0.1 M Na

cacodylate buffer) for 24 h. The tissue was post-fixed with 1% OsO_4 and 0.01% potassium dichromate (same buffer, 1–2 h, RT) dehydrated in graded solutions of ethanol (10 min each) and then 100% acetone (three changes 10 min each). Specimens were embedded in epoxy resin (Epon 812/AralditeM) as detailed earlier [25]. A total of 60–70 nm thick serial sections were cut (2–5% ethanol in water), allowed to form a ribbon on the bath surface and collected with Pioloform-coated slot copper grids. Sections were counterstained with saturated ethanolic uranyl acetate, followed by lead citrate, and were then placed in a rotating grid holder to allow uniform orientation of sections on adjacent grids in the electron microscope. Electron micrographs (6000×) were obtained in a JEOL 1010 electron microscope from the medial molecular layer of dentate gyrus, at a distance of 80–100 µm from the layer of neuronal cell bodies. Up to 100 serial sections per series were photographed. A cross-sectioned myelinated axon, mitochondria and dendrites spanning each section provided a fiduciary reference for initial alignment of serial sections.

(c) Three-dimensional reconstruction and morphometry

Digital electron micrographs (1200 dpi) were aligned using SEM Align 1.26 and contours of individual dendritic spines, PSDs and astrocytic processes were traced digitally using IGL Trace 1.26 (http://www.synapses.clm.utexas.edu/). Section thickness was determined as described earlier [26] and was normally 60–70 nm (grey/white colour). Volumes and surface areas of individual structures were computed and three-dimensional (3D) objects were generated using the IGL Trace. Dendritic spines adjacent to identified astrocytic processes were reconstructed and analysed (see Results). Additional criteria for 'mushroom' spines were the presence of a spine apparatus and a complex PSD (perforated, U-shaped or segmented) whereas 'thin' spines had only macular PSDs and no spine apparatus [27,28].

For distance measurements, we used reconstructed surfaces represented by quasi-regular triangular lattices; lattice vertices provided a set of surface coordinates. Where required, centroids were calculated directly from such sets. Running through and measuring all distances between PSDs (all surface points) and the astrocyte membrane (all surface points with an upper distance limit) was carried out in 3D using the IGL Trace; the distance metric was Euclidean throughout. We exported 3D reconstructions to the 3D-Studio-Max 8 software for surface rendering. Statistica (StatSoft) was used for statistical testing. ANOVAs followed by Bonferroni's or Tukey's (unequal samples) tests were performed using OriginPro v. 7.5.

3. Results

(a) Astrocytes in dentate gyrus: neuropil volume fraction in live tissue

To understand architectonics and space-filling features of individual astrocytes in dentate gyrus, we carried out single-cell experiments in acute hippocampal slices. We applied visual patch-clamp routines to identify individual astrocytes (occurring preferentially in the medial perforant path layer), filling them, in whole-cell mode, with the fluorescent tracer Alexa Fluor 594. To restrict indicator diffusion to individual cells, gap junctions were blocked by carbenoxolone (Materials and methods). Astrocytes were visualized in serial stacks of fluorescence images obtained with two-photon (2P) excitation of Alexa (figure 1*a*). Stable fluorescence was usually achieved within 5–10 min (access resistance typically approx. 10 MOhm). Pictures were taken about 20 min after entering whole-cell. All recorded cells were electrically passive: the average resting V_m and the input resistance were, respectively, -88.1 ± 0.7 mV and 5.9 ± 1.1 MOhm (mean $\pm$ s.e.m., $n = 10$; figure 1*b*; electronic supplementary material, figure S1), reflecting the properties of regular 'passive' astrocytes [29]. Cell morphology was consistent with that reported in the same area using Lucifer Yellow staining [24], including a proportion of astrocytes with long dendrite-like trunks (figure 1*a*). The average cross-sectional area occupied by an individual astrocyte arbour was 2631 ± 268 µm^2 ($n = 10$); this corresponded to an average caliper size of 57.8 ± 18.5 µm, consistent with previous reports [30].

The tissue volume fraction occupied by glia, G_V, should reflect basic properties of glutamate uptake in the area. G_V has hitherto been measured in fixed preparations using stereological rules [2,6]. To measure G_V in live tissue, we applied 2P microscopy: 2P excitation occurs entirely within the approximately 1 µm thick optical layer ensuring that no contaminating fluorescence is generated outside the focal plane. Because glial protrusions are normally much thinner than the translucent excitation layer, the sampled emission $F(i,j)$ (i and j, pixel coordinates in the X–Y plane) is proportional to the local volume fraction of indicator-filled glia, or $G_V(i,j)$.

To translate $G_V(i,j)$ into the local volume fraction, we related it to the fluorescence $F_{max}(i,j)$ inside the dye-filled cell soma (i.e. 100% volume fraction) in the same focal plane (figure 1*c*): $G_V(i,j) = (F(i,j) - F_0)/(F_{max} - F_0)$ where F_0 is background fluorescence (outside any stained structures). We used this approach to obtain two measurements. First, we excluded the areas occupied by the soma and thick (more than 1 µm) astrocyte processes. The resulting average value $G_V^{min} = 4.0 \pm 0.3\%$ ($n = 10$ cells) thus reflected the tissue volume fraction occupied by the fine glial protrusions. Importantly, local $G_V^{min}(i,j)$ was relatively constant away from the soma (figure 1*c*), suggesting homogeneous glial coverage throughout the astrocyte domain. Second, we measured the G_V value that included all dendrite-like processes: $G_V = 8.9 \pm 0.7\%$ ($n = 10$). This value should correspond to electron microscopy observations in which fragments of astrocyte processes are sampled arbitrarily. Because hippocampal astrocytes tend to occupy separate neuropil domains, with little or no spatial overlap [24,30,31], the value of G_V should therefore provide control for the completeness of astroglia reconstruction at the electron microscopy level.

(b) Spatial juxtaposition of synapses and glia

In serial-section electron micrographs of medial molecular layer (Materials and methods), we identified glial fragments using the criteria described earlier [3,6,11,32] and further validated this by tracing contiguous structures across the series (figure 2*a*; electronic supplementary material, figure S2). Throughout the sample, the average tissue volume fraction occupied by glia was $G_V = 9.18 \pm 0.65\%$ ($n = 16$ astrocyte fragments). This was in excellent agreement with G_V measured in live tissue (see above), indicating the accuracy of glial identification. We next reconstructed fragments of astrocytes together with the adjacent dendritic spines containing PSDs (figure 2*b*; electronic supplementary material, figure S2).

In 3D reconstructions, we could unambiguously distinguish between thin ($n = 136$) and mushroom ($n = 53$) dendritic spines (figure 2*c*–*d*), which differ more than fivefold in their average head volume [14,21,25]. Indeed, the average

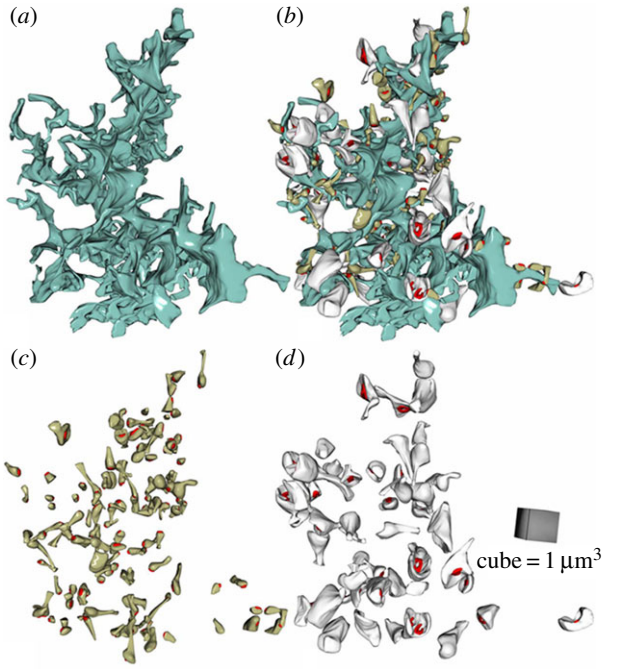

Figure 2. Three-dimensional reconstruction of contiguous astrocyte fragments with adjacent synapses. (*a–d*) A fragment of a dentate astrocyte reconstructed in three dimensions (blue, (*a*,*b*)) together with the adjacent dendritic spines (grey and dark yellow structures, (*b*)) equipped with PSDs (red). The spines are unambiguously separated into the sub-groups of thin (dark yellow, shown separately in (*c*)) and mushroom (grey, (*d*)). See the electronic supplementary material, figure S2, for examples of the original serial sections with identified structures.

head volume for mushroom and thin spines was, respectively, 0.1998 ± 0.0156 and $0.0323 \pm 0.0019\ \mu m^3$ (mean $\pm$ s.e.m.). An average 3D nearest-neighbour distance between the PSD centroids among all spines was $0.57 \pm 0.02\ \mu m$ ($n = 190$). This was consistent with the volume density of excitatory synapses in dentate gyrus [33,34], and similar to the average nearest-neighbour inter-synaptic distance in area CA1 [10,35]. This consistency further validated the accuracy of reconstruction procedures.

First, we attempted to gauge glial coverage of synapses by calculating the proportion of synaptic circumvent approached by glia [10,11] (electronic supplementary material, figure S3). However, in some cases glial protrusions penetrated inside the synaptic apposition zone (electronic supplementary material, figure S4) whereas in other cases classifying the glia-circumvent 'contact' did not appear unambiguous (electronic supplementary material, figure S3). We therefore concentrated on an unsupervised methodology and calculated minimal (edge-to-edge) 3D distances between each individual PSD and the nearest astrocyte membrane, D_{min}. To minimize bias associated with 3D-surface rendering, D_{min} was measured using non-smoothed coordinates (3.6 nm/pixel resolution; figure 3*a*). Perhaps unexpectedly, we found that the distributions of D_{min} for the sub-populations of mushroom and thin spines were markedly different (figure 3*b*): the average D_{min} values were, respectively, 145 ± 9 nm and 77 ± 6 nm ($n = 53$ and 156; $p < 0.001$). Glial protrusions occur therefore twice as close to the PSDs on thin dendritic spines in comparison to those on mushroom spines.

However, D_{min} does not necessarily represent the whole glial environment: for instance, closely approaching thin protrusions might connect to the bulk of distant glia. We therefore developed an integrative measure that would indicate how much glial surface how closely approaches each PSD. Because the closer glial surfaces are to the PSD the stronger impact they must have on any diffusion-mediated glia–synapse communication (figure 3*c*), we weighted all PSD–glia distances accordingly. The chosen weight function $w(r) = A \times \exp(-18r^2)$ approximated the drop of transmitter concentration at a distance r from the release site shortly post-release [6,9], with the factor A normalizing the sum of all weights as one: $A^{-1} = \int_0^\infty w(r)\,dr$. For each PSD, therefore, we calculated the average weighted PSD–glia distance $D_w = \int_0^{r_{max}} w(r) r\,dr$ that incorporates information about all glial surfaces occurring at $r < r_{max}$ from the PSD ($r_{max} = 0.5\ \mu m$ corresponded to the average distance to the next PSD).

The average D_w for mushroom and thin spines, respectively, was $0.385 \pm 0.006\ \mu m$ and $0.276 \pm 0.005\ \mu m$ ($p < 0.001$) when D_w was referred to the PSD centroid and $0.324 \pm 0.004\ \mu m$ and $0.264 \pm 0.004\ \mu m$ ($p < 0.001$) when D_w was referred to all points on the surface of each PSD. This result indicated that astroglia approached PSDs on thin dendritic spines more closely than PSDs on mushroom spines. (Additional calculations indicated that this difference was relatively insensitive to a particular form of $w(r)$.)

4. Discussion

Here, we have analysed fine 3D architectonics of astrocyte compartments and adjacent excitatory synapses in the dentate neuropil. We have found that on average astroglia are significantly nearer to synapses on thin dendritic spines compared with those on mushroom spines. What could be the adaptive significance of this difference?

2P uncaging of glutamate at sub-synaptic resolution provided a map of AMPA receptor (AMPAR) distribution in dendritic spines visualized in hippocampal pyramidal neurons [16]. The authors showed that AMPARs are abundant (up to 150 per spine) in mushroom spines but are scarcely present in thin spines or filopodia of dendrites. This observation was consistent with the molecular machinery that controls, in a synergistic manner, both dendritic spine elongation and the pruning of local AMPARs in cultured cortical neurons [20]. In agreement with this, dendritic spines with larger, complex PSDs showed greater numbers of immuno-gold labelled AMPARs compared with spines with simple, macular PSDs in hippocampal neurons [17]. Remarkably, induction of long-term potentiation (LTP) by local glutamate uncaging could transform, in real time, thin spines deficient in AMPARs into the AMPAR-enriched large, mushroom-type spines [19]. Furthermore, classical electrophysiological observations propose that LTP may turn NMDA receptor-dominated ('silent') synapses into synapses relying on AMPAR-mediated transmission [36,37], evoking a concept of 'learning spines' as opposed to 'memory spines' [21,38].

This functional distinction between the two spine types may provide one possible explanation for tighter and snugger glial coverage around thin spines. In contrast to low-affinity AMPARs, high-affinity synaptic NMDA receptors could in some conditions sense glutamate released outside the immediate synapse [7,9]. This 'spill-in' signal is controlled by high-affinity glial glutamate transporters [2,4,39], which

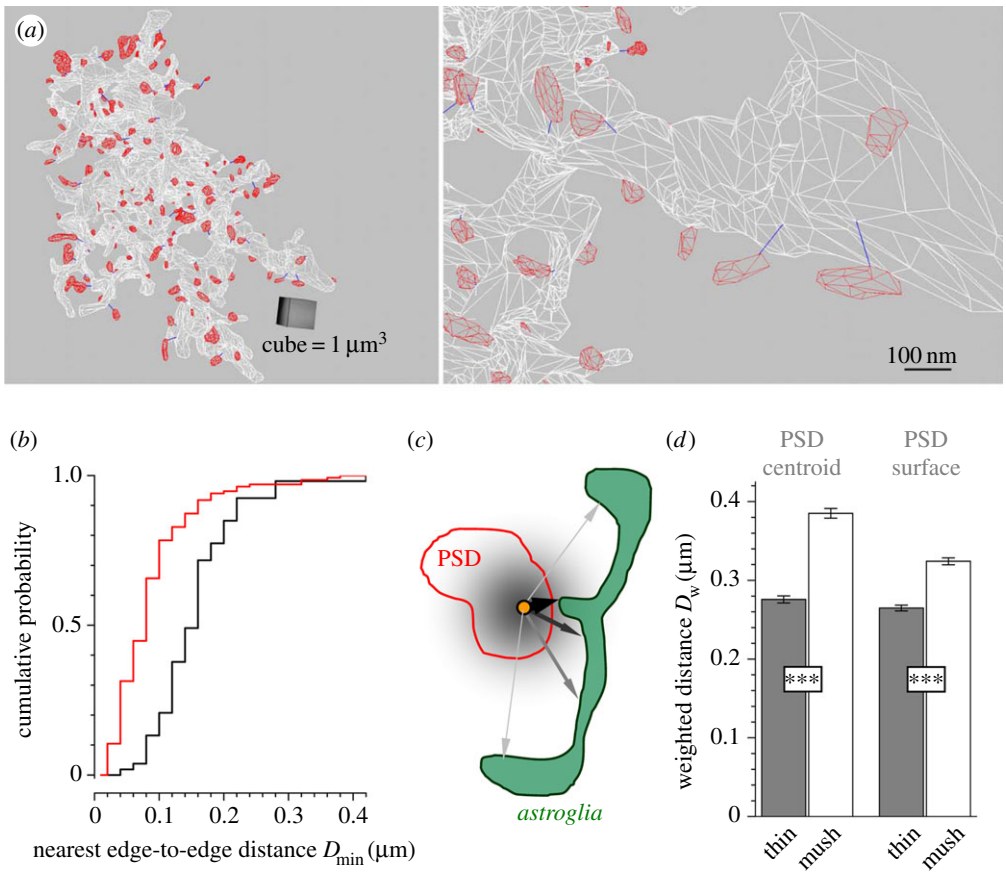

Figure 3. Astrocyte membranes are much closer to the PSDs occurring on thin, compared to mushroom, dendritic spines. (*a*) A diagram illustrating automatic measurement of the nearest edge-to-edge distances D_{min} between all individual PSDs (red mesh) and astrocyte membranes (white mesh) in space, at two levels of detail. Blue segments show D_{min} determined in 3D automatically; smooth surface rendering (as in figure 2) is omitted for clarity. (*b*) Distribution (cumulative probability plot) of D_{min} for individual PSDs occurring on thin (red, $n = 136$) and mushroom (black, $n = 53$) dendritic spines. (*c*) A two-dimensional diagram illustrating a rationale behind the weighting of PSD–glia distances. Distances between PSD (red, either the centroid only or all surface points) and all points on the surface of a neighbouring glial process (green) are measured, with larger distances bearing less weight (indicated by arrow thickness and shade of grey). The weighting reflects a rapid drop of transmitter concentration with distance from the site of release (yellow dot). See Results for details. (*d*) Grey and white columns, average ($\pm$ s.e.m.) weighted PSD–astroglia distances D_w for thin and mushroom dendritic spines, respectively, measured with respect to either PSD centroids or all PSD surface points, as indicated (***$p < 0.001$).

could thus be particularly important for synapses that rely on high-affinity (NMDA) receptors.

The important adaptive role for the extent of synaptic glial coverage could also arise from the findings that hippocampal astrocytes can exchange transmitter signals with the neighbouring neurons [40,41]. Because such signalling relies on rapid extracellular diffusion outside the synaptic cleft, changes in the spatial juxtaposition of synapses and glia should have a direct impact on this mode of neuron–glia communication [12,13].

Funding statement. This work was supported by BBSRC (BB/J021687/1), the Wellcome Trust, Medical Research Council (UK), European Union (FP6 Promemoria 512012), ERC Advanced Grant, NRW-Rückkehrerprogramm, Human Frontiers Science Program (HFSP RGY-0084/2012) and UCL Excellence Fellowship.

References

1. Bergles DE, Jahr CE. 1998 Glial contribution to glutamate uptake at Schaffer collateral–commissural synapses in the hippocampus. *J. Neurosci.* **18**, 7709–7716.
2. Lehre KP, Danbolt NC. 1998 The number of glutamate transporter subtype molecules at glutamatergic synapses: chemical and stereological quantification in young adult rat brain. *J. Neurosci.* **18**, 8751–8757.
3. Danbolt NC. 2001 Glutamate uptake. *Progr. Neurobiol.* **65**, 1–105. (doi:10.1016/S0301-0082(00)00067-8)
4. Diamond JS. 2001 Neuronal glutamate transporters limit activation of NMDA receptors by neurotransmitter spillover on CA1 pyramidal cells. *J. Neurosci.* **21**, 8328–8338.
5. Herman MA, Jahr CE. 2007 Extracellular glutamate concentration in hippocampal slice. *J. Neurosci.* **27**, 9736–9741. (doi:10.1523/JNEUROSCI.3009-07.2007)
6. Lehre KP, Rusakov DA. 2002 Asymmetry of glia near central synapses favors presynaptically directed glutamate escape. *Biophys. J.* **83**, 125–134. (doi:10.1016/S0006-3495(02)75154-0)
7. Arnth-Jensen N, Jabaudon D, Scanziani M. 2002 Cooperation between independent hippocampal synapses is controlled by glutamate uptake. *Nat. Neurosci.* **5**, 325–331. (doi:10.1038/nn825)
8. Lozovaya NA, Grebenyuk SE, Tsintsadze T, Feng B, Monaghan DT, Krishtal OA. 2004 Extrasynaptic NR2B and NR2D subunits of NMDA receptors shape 'superslow' afterburst EPSC in rat hippocampus. *J. Physiol.* **558**, 451–463. (doi:10.1113/jphysiol.2004.063792)
9. Scimemi A, Fine A, Kullmann DM, Rusakov DA. 2004 NR2B-containing receptors mediate cross talk among hippocampal synapses. *J. Neurosci.* **24**, 4767–4777. (doi:10.1523/JNEUROSCI.0364-04.2004)
10. Ventura R, Harris KM. 1999 Three-dimensional relationships between hippocampal synapses and astrocytes. *J. Neurosci.* **19**, 6897–6906.

11. Witcher MR, Kirov SA, Harris KM. 2007 Plasticity of perisynaptic astroglia during synaptogenesis in the mature rat hippocampus. *Glia* **55**, 13–23. (doi:10.1002/glia.20415)
12. Oliet SHR, Piet R, Poulain DA. 2001 Control of glutamate clearance and synaptic efficacy by glial coverage of neurons. *Science* **292**, 923–926. (doi:10.1126/science.1059162)
13. Piet R, Vargova L, Sykova E, Poulain DA, Oliet SH. 2004 Physiological contribution of the astrocytic environment of neurons to intersynaptic crosstalk. *Proc. Natl Acad. Sci. USA* **101**, 2151–2155. (doi:10.1073/pnas.0308408100)
14. Harris KM, Jensen FE, Tsao B. 1992 Three-dimensional structure of dendritic spines and synapses in rat hippocampus (CA1) at postnatal day 15 and adult ages: implications for the maturation of synaptic physiology and long-term potentiation. *J. Neurosci.* **12**, 2685–2705.
15. Kirov SA, Sorra KE, Harris KM. 1999 Slices have more synapses than perfusion-fixed hippocampus from both young and mature rats. *J. Neurosci.* **19**, 2876–2886.
16. Matsuzaki M, Ellis-Davies GC, Nemoto T, Miyashita Y, Iino M, Kasai H. 2001 Dendritic spine geometry is critical for AMPA receptor expression in hippocampal CA1 pyramidal neurons. *Nat. Neurosci.* **4**, 1086–1092. (doi:10.1038/nn736)
17. Ganeshina O, Berry RW, Petralia RS, Nicholson DA, Geinisman Y. 2004 Differences in the expression of AMPA and NMDA receptors between axospinous perforated and nonperforated synapses are related to the configuration and size of postsynaptic densities. *J. Comp. Neurol.* **468**, 86–95. (doi:10.1002/cne.10950)
18. Medvedev NI, Rodriguez-Arellano JJ, Popov VI, Davies HA, Tigaret CM, Schoepfer R, Stewart MG. 2008 The glutamate receptor 2 subunit controls post-synaptic density complexity and spine shape in the dentate gyrus. *Eur. J. Neurosci.* **27**, 315–325. (doi:10.1111/j.1460-9568.2007.06005.x)
19. Matsuzaki M, Honkura N, Ellis-Davies GC, Kasai H. 2004 Structural basis of long-term potentiation in single dendritic spines. *Nature* **429**, 761–766. (doi:10.1038/nature02617)
20. Xie Z, Huganir RL, Penzes P. 2005 Activity-dependent dendritic spine structural plasticity is regulated by small GTPase Rap1 and its target AF-6. *Neuron* **48**, 605–618. (doi:10.1016/j.neuron.2005.09.027)
21. Bourne J, Harris KM. 2007 Do thin spines learn to be mushroom spines that remember? *Curr. Opin. Neurobiol.* **17**, 381–386. (doi:10.1016/j.conb.2007.04.009)
22. Emptage NJ, Reid CA, Fine A, Bliss TV. 2003 Optical quantal analysis reveals a presynaptic component of LTP at hippocampal Schaffer-associational synapses. *Neuron* **38**, 797–804. (doi:10.1016/S0896-6273(03)00325-8)
23. Scott R, Rusakov DA. 2006 Main determinants of presynaptic Ca^{2+} dynamics at individual mossy fiber-CA3 pyramidal cell synapses. *J. Neurosci.* **26**, 7071–7081. (doi:10.1523/JNEUROSCI.0946-06.2006)
24. Isokawa M, McKhann II GM. 2005 Electrophysiological and morphological characterization of dentate astrocytes in the hippocampus. *J. Neurobiol.* **65**, 125–134. (doi:10.1002/neu.20186)
25. Popov VI, Davies HA, Rogachevsky VV, Patrushev IV, Errington ML, Gabbott PL, Bliss TV, Stewart MG. 2004 Remodelling of synaptic morphology but unchanged synaptic density during late phase long-term potentiation (LTP): a serial section electron micrograph study in the dentate gyrus in the anaesthetised rat. *Neuroscience* **128**, 251–262. (doi:10.1016/j.neuroscience.2004.06.029)
26. Fiala JC, Harris KM. 2001 Cylindrical diameters method for calibrating section thickness in serial electron microscopy. *J. Microsc.* **202**, 468–472. (doi:10.1046/j.1365-2818.2001.00926.x)
27. Popov V, Stewart MG. 2009 Complexity of contacts between synaptic boutons and dendritic spines in adult mammalian hippocampus: three-dimensional reconstructions from serial ultrathin sections *in vivo*. *Synapse* **63**, 369–377. (doi:10.1002/syn.20613)
28. Stewart MG, Popov V, Kraev IV, Medvedev N, Davies HA. 2014 Structure and complexity of the synapse and dendritic spine, ch. 1. In *The synapse: structure and function* (eds V Pickel, M Segal), pp 1–20. Amsterdam, The Netherlands: Academic Press.
29. Volterra A, Meldolesi J. 2005 Astrocytes, from brain glue to communication elements: the revolution continues. *Nat. Rev. Neurosci.* **6**, 626–640. (doi:10.1038/nrn1722)
30. Ogata K, Kosaka T. 2002 Structural and quantitative analysis of astrocytes in the mouse hippocampus. *Neuroscience* **113**, 221–233. (doi:10.1016/S0306-4522(02)00041-6)
31. Bushong EA, Martone ME, Jones YZ, Ellisman MH. 2002 Protoplasmic astrocytes in CA1 stratum radiatum occupy separate anatomical domains. *J. Neurosci.* **22**, 183–192.
32. Bernardinelli Y, Muller D, Nikonenko I. 2014 Astrocyte-synapse structural plasticity. *Neural Plast.* **2014**, 1–13. (doi:10.1155/2014/232105)
33. Geinisman Y, de Toledo-Morrell L, Morrell F, Persina IS, Rossi M. 1992 Structural synaptic plasticity associated with the induction of long-term potentiation is preserved in the dentate gyrus of aged rats. *Hippocampus* **2**, 445–456. (doi:10.1002/hipo.450020412)
34. Rusakov DA, Harrison E, Stewart MG. 1998 Synapses in hippocampus occupy only 1-2% of cell membranes and are spaced less than half-micron apart: a quantitative ultrastructural analysis with discussion of physiological implications. *Neuropharmacology* **37**, 513–521. (doi:10.1016/S0028-3908(98)00023-9)
35. Rusakov DA, Kullmann DM. 1998 Extrasynaptic glutamate diffusion in the hippocampus: ultrastructural constraints, uptake, and receptor activation. *J. Neurosci.* **18**, 3158–3170.
36. Liao DZ, Hessler NA, Malinow R. 1995 Activation of postsynaptically silent synapses during pairing-induced LTP in CA1 region of hippocampal slice. *Nature* **375**, 400–404. (doi:10.1038/375400a0)
37. Isaac JTR, Nicoll RA, Malenka RC. 1995 Evidence for silent synapses: implications for the expression of LTP. *Neuron* **15**, 427–434. (doi:10.1016/0896-6273(95)90046-2)
38. Segal M. 2010 Dendritic spines, synaptic plasticity and neuronal survival: activity shapes dendritic spines to enhance neuronal viability. *Eur. J. Neurosci.* **31**, 2178–2184. (doi:10.1111/j.1460-9568.2010.07270.x)
39. Bergles DE, Diamond JS, Jahr CE. 1999 Clearance of glutamate inside the synapse and beyond. *Curr. Opin. Neurobiol.* **9**, 293–298. (doi:10.1016/S0959-4388(99)80043-9)
40. Jourdain P *et al*. 2007 Glutamate exocytosis from astrocytes controls synaptic strength. *Nat. Neurosci.* **10**, 331–339. (doi:10.1038/nn1849)
41. Perea G, Araque A. 2007 Astrocytes potentiate transmitter release at single hippocampal synapses. *Science* **317**, 1083–1086. (doi:10.1126/science.1144640)